EVALUATION OF THE SU2 OPEN-SOURCE CODE FOR A HYPERSONIC FLOW AT MACH NUMBER 5

Jia-Ming Yeap
Centre for Computational Engineering Sciences, Cranfield University, Cranfield, Bedfordshire, MK43 0AL, United Kingdom
jmryan93@gmail.com

Zeeshan A. Rana
Centre for Aeronautics, Cranfield University, Cranfield, Bedfordshire, MK43 0AL, United Kingdom
zeeshan.rana@cranfield.ac.uk

László Könözsy
Centre for Computational Engineering Sciences, Cranfield University, Cranfield, Bedfordshire, MK43 0AL, United Kingdom
laszlo.konozsy@cranfield.ac.uk

Karl W. Jenkins
Centre for Computational Engineering Sciences, Cranfield University, Cranfield, Bedfordshire, MK43 0AL, United Kingdom
k.w.jenkins@cranfield.ac.uk

Abstract. This paper presents the evaluation of the Stanford University Unstructured (SU2) open-source computational software package for a high Mach number 5 flow. The test case selected is an impinging shock wave turbulent boundary layer interaction (SWTBLI) on a flat plate where the experimental data of Schülein et al. [27] is used for validation purposes. Two turbulence models, the Spalart–Allmaras (SA) and the k-ω Shear Stress Transport (SST) within the SU2 code are evaluated in this study. Flow parameters, such as skin friction, wall pressure distribution and boundary layer profiles are compared with experimental values. The results demonstrate the performance of the SU2 code at a high Mach number flow and highlight its limitations in predicting fluid flow physics. At higher shock generator angles, the discrepancy between experimental and CFD data is more significant. Within the interaction and flow separation zones, a smaller separation bubble and delayed separation are predicted by the SA model while the k-ω SST model predicts early separation. Both models are able to predict wall pressure distribution correctly within the experimental values. However, discrepancies were observed in the prediction of skin friction due to the inability of the models to capture the boundary layer recovery after shock impingement.

1. Introduction

A hypersonic air-breathing propulsion (HAP) device scoops air from the atmosphere to generate thrust [1], in contrast to a rocket propulsion engine where on-board liquid oxygen is utilized for combustion. The obvious advantage of a HAP device is the reduction in payload requirement (on-board oxygen) for the aircraft; however, such propulsion systems suffer from low performance at subsonic speeds, and thus are dependent on other propulsion devices for the take-off procedure [2]. Ramjet and scramjet are both HAP devices used for flights above sonic conditions; combustion in a ramjet occurs at subsonic speeds, while for the scramjet combustion is carried out at supersonic speeds. The concept of scramjet engines was first devised around the 1950s [3], a period of time when the capability of Computational Fluid Dynamics (CFD) was very limited. The first successful flight of a scramjet engine, named HyShot-II and built at the University of Queensland, took place in July of 2002 [4]. Further experiments were conducted [5, 6] and detailed computational investigations have also been performed on the HyShot-II scramjet. Karl et al. [7] was perhaps the first to present the experimental investigations on the overall flow field of the HyShot-II and validated their findings through RANS (Reynolds-Averaged Navier–Stokes) modeling. This was followed by several further investigations on the same geometry. Berglund et al. [8], Fureby et al. [9] and Chapuis et al. [10] investigated the supersonic combustion phenomenon inside the HyShot-II scramjet combustor using both the time-averaged RANS and the time-accurate LES (Large Eddy Simulations) turbulence modeling approaches. You et al. [11] presented a detailed investigation on the fuel injection and mixing inside the same combustor to extend the understanding through RANS and DES (Detached Eddy Simulation) formulations. Many further studies have since been carried out [12, 13, 14] to further understand the flow dynamics around and inside the HyShot-II geometry. Owing to the complexities associated with the scramjet, a more generic model of the supersonic flow inside the combustion chamber with transverse sonic jet injection [15, 16, 17] was used to understand the complex flow characteristics and mixing of air with fuel where Shock Wave Turbulent Boundary Layer Interactions (SWTBLI) also play a major role.

One complex flow phonomenon in a supersonic combustion chamber is the SWTBLI. Typical applications of SWTBLI include supersonic/hypersonic engines, inlets of high speed air-breathing propulsion vehicles and high Mach number flows over control surfaces [18, 19]. Although efforts were exerted at the design stage to avoid any shock wave entering the combustion chamber of the HyShot-II [7, 12], a shock train was observed traveling inside the combustion chamber giving rise to the SWTBLI phenomenon. This type of interaction causes the boundary layer to separate and develop recirculation of flow. As the scramjet employs auto-ignition, this recirculation can have an effect on the combustion process and even results in unsteady unstart in HyShot-II [12, 13]. Shock wave boundary layer interaction can have ahuge influence on the nature of high Mach number flows, compromising the safety and risk management for a specific industrial system such as a supersonic engine inlet. The interaction between shocks and boundary layer can cause an abrupt deceleration in fluid flow

and thickening of the turbulent boundary layer [20]. In the separation zone, three-dimensional effects in the form of Goertler vortices have also been reported by several researchers [21, 22, 23, 24]. Along with the occurrence of flow separation, high pressure fluctuations and wall heat flux could be observed in the interaction region. The assumption of stable compressive deceleration in the freestream flow into a hypersonic air intake as an isentropic process is invalid in true flight conditions [18].

Most research in this area is still centered around test cases with simple geometries such as a flat plate and shock generator [21]. An impinging SWTBLI on a flat plate is considered as a canonical test case [25], along with some other typical SWTBLI configurations such as compression ramp and expansion-compression corner flows [26]. Schülein et al. [27] conducted detailed experiments on an impinging SWTBLI on a flat plate and presented results for the skin friction and heat transfer measurements, carrying out the experiment in the DLR Ludwieg-Tube (DNW-RNG) wind tunnel facility in Göttingen. The test model consisted of a flat plate of 500 mm in length and 400 mm in width, as well as a shock generator of 300 mm in length and 400 mm in width. In Figure 1, the shock generator is oriented at a shock generator angle β and its leading edge and trailing edge are positioned such that the shock impingement location is always 350 mm from the leading edge of flat plate at all freestream Mach numbers and shock generator angles. A Further comprehensive database of supersonic/hypersonic test cases of a Mach number of at least 3 was also reported [28, 29], ranging from an impinging shock to three-dimensional double fin configurations.
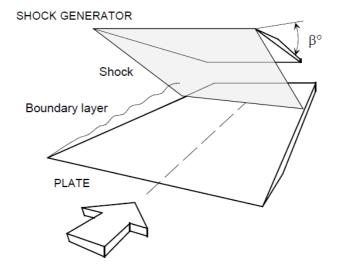

Figure 1. Sketch of the test model from Schülein et al. [27]

Fedorova et al. [30] conducted a CFD analysis of the experiment of Schülein et al. [27] using unsteady Favre-Averaged Navier–Stokes (FANS) equations along with the

k-ω turbulence model of Wilcox [40]. The results demonstrate that the disagreement between numerical and experimental data is greater with increasing interaction strength. At β of 6° and 10°, good agreement is reported for the flow parameters such as skin friction and boundary layer profiles; however, skin friction downstream of the impingement point was underestimated at all angles investigated. Leger and Poggie [31, 32] illustrated both, the weak and the strong interaction cases of an impinging SWTBLI on a flat plate and discussed the nature of the shock wave boundary layer interactions. They also observed the reduction in the wall shear stress and increase in the wall pressure across the SWTBLI region due to a double-shock event in the case of weak interactions. Several more experimental and numerical investigations were carried out for this particular arrangement and its variants. However, the experiment of Schülein et al. [27] remains the fundamental source of data for verification and validation of computational methods and turbulence models [33].

Reynolds-averaged modeling is considered to be a low accuracy approach in predicting skin friction and heat transfer distributions while it performs better in modeling primary separation and pressure fields. In a strong interaction case, the agreement of experimental and CFD data is reduced. This paper presents an attempt to evaluate the Stanford University Unstructured (SU2) open-source CFD software package [34, 35, 36] using compressible Reynolds-averaged turbulence modeling approaches for an impinging SWTBLI on flat plate at Mach number of 5 in comparison with the experimental data of Schülein et al. [27]. The main objective here is the validation of the numerical results performed with the use of the SU2 code for an impinging SWTBLI case at Mach number 5. Furthermore, another goal is to understand the limitations of the SU2 code for the investigations of complex flow phenomena of SWTBLI at a high Mach number flow. In this study, due to the constraint of computational resources for very high-speed flows, two-dimensional simulations have been performed.

2. Methodology and Computational Framework

2.1. **The SU2 open-source code.** The SU2 code is an open-source Computational Fluid Dynamics (CFD) software package, first developed by Aerospace Design Laboratory at Stanford University. One of the motivations behind the SU2 code is to solve problems which involve discretization of Partial Differential Equations (PDEs) such as Navier-Stokes and optimization of PDE-constrained problems. It is a software collection based on programming languages such as C++, Python, OpenMPI and Metis. Gradient-based adjoint solver capability is included in the development of the SU2 code through mesh adaption process driven by a specific function such as lift or drag. The SU2 code is based on Finite Volume (FV) or Finite Element (FE) methods and complete description of the SU2 code along with its structure can be found in [34, 35, 36]. Since the first introduction of the SU2 open-source code, it has been validated for a number of benchmark cases such as low Mach flows over an NACA0012 aerofoil [34, 35], supersonic or hypersonic flow regimes [34] as in a Lockheed N+2 aircraft at Mach number of 1.7, and the RAM-C II flight test vehicle at the Mach number of 16 with a plasma solver including additional sets of equations and source terms to take into account non-equilibrium effects [36].

2.2. **Governing equations of high-speed compressible flows.** The governing equations of high-speed compressible, viscous, heat-conducting flows, i.e., the instantaneous mass, momentum and enegy conservation equations, are considered [40] as

$$\frac{\partial \rho}{\partial t} + \frac{\partial}{\partial x_i}\left(\rho u_i\right) = 0, \tag{2.1}$$

$$\frac{\partial}{\partial t}\left(\rho u_i\right) + \frac{\partial}{\partial x_j}\left(\rho u_i u_j\right) = -\frac{\partial p}{\partial x_j} + \frac{\partial \tau_{ij}}{\partial x_j}, \tag{2.2}$$

$$\frac{\partial}{\partial t}\left(\rho E\right) + \frac{\partial}{\partial x_j}\left(\rho u_j E\right) = -\frac{\partial}{\partial x_j}\left(p u_j\right) + \frac{\partial}{\partial x_j}\left(u_i \tau_{ij} + \lambda \frac{\partial T}{\partial x_j}\right), \tag{2.3}$$

where ρ is the fluid density, u_i is the component of the velocity vector ($i = 1,2$ for two-dimensional and $i = 1,2,3$ for three-dimensional problems), p is the pressure field which is a function of the density, τ_{ij} describes the components of the viscous stress tensor, E is the total energy per unit mass, λ is the thermal conductivity, and T is the temperature. The elements of the viscous stress tensor can be expressed by

$$\tau_{ij} = \mu \left(\frac{\partial u_i}{\partial x_j} + \frac{\partial u_j}{\partial x_i}\right) - \frac{2}{3}\mu \frac{\partial u_k}{\partial x_k}\delta_{ij}, \tag{2.4}$$

where μ is the temperature dependent dynamic viscosity of the fluid, and δ_{ij} is the Kronecker delta ($\delta_{ij} = 1$ when $i = j$ and $\delta_{ij} = 0$ when $i \neq j$). For an ideal (perfect) gas, the relationship among pressure, density and temperature in the governing equations (2.1)–(2.3) can be computed by the equation of state as

$$p = \rho R T, \tag{2.5}$$

where R is the perfect (ideal) gas constant. The thermal conductivity λ in the energy equation (2.3) can be expressed by

$$\lambda = \frac{\mu c_p}{Pr}, \tag{2.6}$$

where c_p is the specific heat, and Pr is the dimensionless Prandtl number. In the thermal conductivity λ expression (2.6), the specific heat can be computed as

$$c_p = \frac{\gamma R}{\gamma - 1}, \tag{2.7}$$

where γ is the specific heat ratio. In this numerical study, the SU2 code has been used for solving the Reynolds-Averaged Navier–Stokes (RANS) equations, i.e., the instantaneous governing Eqs. (2.1)–(2.3) after Reynolds-averaging. Therefore, the effective viscosity μ_{eff} is introduced instead of the dynamic viscosity μ of the fluid for turbulence modeling. In that case, the effective viscosity μ_{eff} can be decomposed into the sum of the dynamic μ and the turbulent eddy viscosity μ_t as

$$\mu_{eff} = \mu + \mu_t. \tag{2.8}$$

The effective thermal conductivity λ_{eff} can also be introduced for turbulence modeling purposes and can be decomposed into two parts as follows:

$$\lambda_{eff} = \frac{\mu}{Pr} + \frac{\mu_t}{Pr_t}, \tag{2.9}$$

where Pr_t is the turbulent Prandtl number. Note that in a compressible fluid flow solver, the Sutherland law has to be satisfied by dynamic viscosity μ and turbulent eddy viscosity μ_t, which are included in the appropriately chosen turbulence models. Based on user preferences, the SU2 solver can be configured to perform computations in either dimensional or non-dimensional form. A wide selection of boundary conditions is available in the SU2 compressible solver, including Euler-type wall (inviscid), no-slip wall with isothermal and adiabatic options, symmetry wall, far-field and periodic boundary conditions. At the inlet and outlet sections and surfaces, characteristic-based boundary conditions such as mass flow rate, supersonic inlet properties, stagnation conditions, back pressure at the outlet and supersonic outlet can be prescribed. Two engineering turbulence models are available in the SU2 code which are evaluated in the present numerical study, namely the Spalart–Allmaras (SA) one-equation turbulence model [37] and the k-ω Shear Stress Transport (SST) model of Menter [38], which are based on Boussinesq hypothesis and whose basic concepts are described briefly subsequently. In the present study, for the sake of simplicity and due to the constraint of computational resources for very high-speed flows, two-dimensional simulations have been performed and their results are analyzed in comparison with the experimental data of Schülein et al. [27]. The motivation of this study is to analyze the behavior of the SU2 open-source CFD code for high Mach numbers, where a knowledge gap still exists.

2.2.1. *The Spalart–Allmaras (SA) turbulence model.* A linear relationship between the turbulent Reynolds shear stresses and the mean velocity gradients is assumed in the Boussinesq eddy viscosity hypothesis, and the SA one-equation turbulence model neglects the contribution of the turbulent kinetic energy (TKE) k in the Reynolds stress tensor. Therefore, the turbulent Reynolds shear stress can be expressed by

$$\overline{u'v'} = -\nu_t \left(\frac{\partial U}{\partial y} + \frac{\partial V}{\partial x} \right), \tag{2.10}$$

where U and V are averaged velocity components in y and x spatial directions for two-dimensional flows. In the SA model, turbulent eddy viscosity is predicted through a new variable $\widehat{\nu}$ which is considered as a transport quantity in the model. This means that an additional transport equation for the scalar variable $\widehat{\nu}$ has to be solved and a closure function f_{v1} has to be computed in each iteration. The dynamic eddy viscosity coefficient μ_t of the SA semi-empirical turbulence model can be defined by

$$\mu_t = \rho \widehat{\nu} f_{v1}, \tag{2.11}$$

where the closure function can be expressed by

$$f_{v1} = \frac{\chi^3}{\chi^3 + c_{v1}^3}, \quad \text{where} \quad \chi = \frac{\widehat{\nu}}{\nu}. \tag{2.12}$$

For the additional transport equation $\widehat{\nu}$ to be solved in the SA model, the convective and viscous fluxes, as well as the source terms, can be expressed with vector notation as

$$\frac{\partial \widehat{\nu}}{\partial t} + (\mathbf{u} \cdot \nabla) \widehat{\nu} = c_{b1} \hat{S} \widehat{\nu} - c_{w1} f_w \left(\frac{\widehat{\nu}}{d_w} \right)^2 + \frac{1}{\sigma} \nabla \cdot [(\nu + \widehat{\nu}) \nabla \widehat{\nu}] + \frac{c_{b2}}{\sigma} |\nabla \widehat{\nu}|^2, \quad (2.13)$$

where $\mathbf{u}$ is the velocity vector, d_w is the distance to the nearest surface, and the scalar quantity $\hat{S}$ in the production term can be formulated as

$$\hat{S} = \left|\underline{\Omega}\right| + \frac{\widehat{\nu}}{\kappa^2 d_w^2} f_{v2}, \tag{2.14}$$

where $\left|\underline{\Omega}\right|$ is the magnitude of the vorticity tensor. The SA model engineering turbulence model has three closure functions (f_{v1}, f_{v2} and f_w) and a total of eight closure coefficients (c_{b1}, c_{b2}, c_{w1}, c_{w2}, c_{w3}, c_{v1}, σ and κ) recorded in the references [35, 39]. For further details on the SA model, see [37].

2.2.2. *The k-ω Shear Stress Transport (SST) turbulence model.* The k-ω SST turbulence model of Menter [38] is a variant of two-equation k-ω models, which involves zonal or blending approach between the conventional k-ω and the k-ϵ model. In the near-wall region, the standard k-ω model is adopted while the k-ϵ model modified for high Reynolds number flows which is modeling the outer region of the boundary layer. In the k-ω SST model, the eddy viscosity μ_t is defined by

$$\mu_t = \frac{\rho a_1 k}{\max\left(a_1 \omega, S\, F_2\right)}, \tag{2.15}$$

where $S = \sqrt{2 S_{ij} S_{ij}}$ is the magnitude of the rate-of-strain tensor and F_2 is the second blending function. Two additional transport equations for the turbulent kinetic energy k and the specific rate of dissipation ω can be considered as

$$\rho \frac{\partial k}{\partial t} + \rho\left(\mathbf{u} \cdot \nabla\right) k = P_k - \rho \beta^\star \omega k + \nabla \cdot \left[\left(\mu + \sigma_k \mu_t\right) \nabla k\right], \tag{2.16}$$

$$\rho \frac{\partial \omega}{\partial t} + \rho\left(\mathbf{u} \cdot \nabla\right) \omega = \frac{\gamma}{\nu_t} P_\omega - \rho \beta_\star \omega^2 +$$
$$+ \nabla \cdot \left[\left(\mu + \sigma_\omega \mu_t\right) \nabla \omega\right] + 2\rho\left(1 - F_1\right) \frac{\sigma_{\omega 2}}{\omega} \nabla k \cdot \nabla \omega, \tag{2.17}$$

where P_k and P_ω are the production terms of the k and ω transport equations. For turbulence modeling, the values of the constants used in transport Eqs. (2.16) and (2.17), and the relevant blending functions can be found in [38, 40].

2.3. Numerical solution of the governing equations. The SU2 code employs Finite Volume (FV) or Finite Element (FE) methods where the numerical flux terms are computed across the control volumes in a dual grid structure with a standard edge-based algorithm and a median-dual vertex based scheme. The governing equations can be considered in a semi-discretized form as

$$\int_{\Omega_i} \frac{\partial U_i}{\partial t} d\Omega + \sum_{j \in N(i)} \left(\tilde{F}_{ij}^c + \tilde{F}_{ij}^v\right) \Delta A_{ij} - S_U \left|\Omega_i\right| = \int_{\Omega_i} \frac{\partial U_i}{\partial t} d\Omega + R_i(U_i) = 0, \tag{2.18}$$

where U_i is the components of the vector of conservative variables, the convective/advective $\tilde{F}_{ij}^c$ and the viscous/diffusion $\tilde{F}_{ij}^v$ fluxes are predicted at the midpoint of each edge, and S_U represents any additional source terms. The convective terms can be discretized in either an upwind or central scheme while diffusion terms are approximated from the average of flow gradients at each node computed with either Green-Gauss or least-squares methods [34]. Source terms involved in the consideration

of other effects are reconstructed with piecewise constant relations. In the present numerical study, for approximating the convective flux terms, the flux-difference-splitting method of Roe is selected in the SU2 code as

$$\tilde{F}_{ij}^c = \tilde{F}\left(U_i, U_j\right) = \frac{1}{2}\left(\tilde{F}_i^c + \tilde{F}_j^c\right) \cdot \overrightarrow{n}_{ij} - \frac{1}{2}\widetilde{K}\left|\widetilde{\lambda}\right|\widetilde{K}^{-1}(U_i - U_j), \qquad (2.19)$$
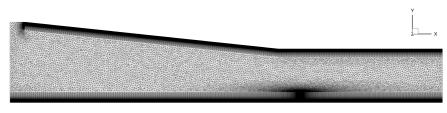
where $\widetilde{\lambda}$ is the local eigenvalue of the scheme. The numerical prediction of convective fluxes is first-order accurate in space while second-order accuracy is achieved with the Monotone Upstream-centered Scheme for Conservation Laws (MUSCL) approximation and slope limiters such as Venkatakrishnan [41] or Barth-Jespersen slope limiter, respectively. In terms of time integration, numerical computations can be performed with implicit and explicit schemes. Although explicit schemes such as Runge-Kutta are available in the SU2 code, the general setup for steady-state problems are carried out with the Euler implicit scheme. The SU2 code employs a local time-stepping approach when each cell moves forward at a different local time step, which is adopted in the numerical setup for faster convergence to steady-state solutions. On the other hand, unsteady problems can be configured with a dual time-stepping approach which can be first- or second-order accurate in time.
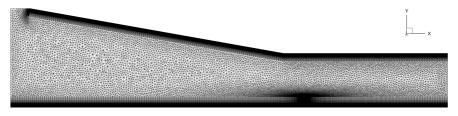
3. Simulation Setup

In this study, compressible Reynolds-averaged simulations have been carried out at three shock generator angles β of 6°, 10°, and 14° as specified in the experimental data of Schülein et al. [27]. The computational domains for each shock generator angle are created according to the coordinates of leading and trailing edges of shock generator as in the experiment of Schülein et al. [27], and two-dimensional (2D) investigations are carried out in this work. For each angle, three levels of meshes are created with the GMSH mesh generator software: coarse, medium and fine. Their description is presented in Table 1. The hybrid meshes are generated at the coarse grid level for each shock generator angle (see Figure 2). Structured quadrilateral cells are created in the boundary layer or near-wall regions of shock generator and the flat plate with y^+ of approximately 1.5 at the medium grid level. The remaining region is then populated with triangular cells, forming an unstructured hybrid meshing strategy. Grid clustering is observed towards the walls and within the region near the shock impingement point for achieving better accuracy in these regions, where $x \approx 0.330 - 0.350\ m$. The grid points in the inflation layer on the bottom wall are clustered towards the shock impingement location (with a growth rate of 1.1) for obtaining better accuracy in the simulations. In the SU2 configuration file, supersonic inlet and outlet boundary conditions are defined at the inlet and outlet sections, respectively. Isothermal no-slip walls are defined for the shock wave generator, flat plate and bottom surfaces while an Euler-type inviscid wall condition is prescribed for the section in front of the leading edge of shock wave generator. The freestream conditions used for the current study are summarized in Table 2.
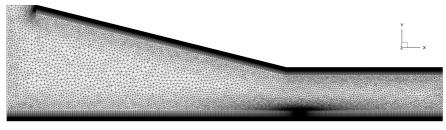
Table 1. Description of two-dimensional hybrid meshes

Mesh	Number of Cells		
	$\beta = 6°$	$\beta = 10°$	$\beta = 14°$
Coarse ($y^+ = 5$)	105 955	106 089	104 495
Medium ($y^+ = 1.5$)	210 954	211 297	209 581
Fine ($y^+ = 0.5$)	405 483	407 584	406 157

(a) Mesh for $\beta = 6°$.

(b) Mesh for $\beta = 10°$.

(c) Mesh for $\beta = 14°$.

Figure 2. 2D coarse meshes for various shock generator angles

Table 2. Freestream conditions

Flow Parameters	Values
Mach Number, Ma	5.0
Unit Reynolds Number, $Re_{1,\infty}$	$3.6736 \cdot 10^6$
Flow Velocity, U_∞	$828.561\ m/s$
Static Pressure, P_∞	$4006.88\ Pa$
Stagnation Pressure, $P_{0,\infty}$	$2.12 \cdot 10^6 Pa$
Static Temperature, T_∞	$68.33\ K$
Stagnation Temperature, $T_{0,\infty}$	$410\ K$
Density, ρ_∞	$0.20428\ kg/m^3$
Dynamic Viscosity, μ_∞	$4.60741 \cdot 10^{-6}\ N \cdot s/m^2$

3.1. **Grid convergence/mesh sensitivity study.** First of all, a grid convergence study is carried out, using Reynolds-averaged turbulence modeling approaches, at the shock generator angle of $\beta=10°$ in a 2D impinging SWTBLI case for both SA and k-ω SST turbulence models. Steady-state solutions are computed with the Euler implicit scheme and a maximum Courant number of $CFL_{max} = 1.0$, where the skin friction coefficients C_f are monitored as a parameter for the Grid Convergence Index (GCI) [42, 43] calculations. At the location of $x = 0.376\ m$, the GCI and the Richardson extrapolation values for skin friction coefficient $C_{f,h=0}$ are computed which are presented in Table 3 and plotted in Figure 3, where h is the normalized wall distance. The obtained computational results for the SA and the k-ω SST turbulence models demonstrate high levels of certainty (96.3% and 105.2%).

Table 3. Grid convergence study on the $\beta=10°$ case

Turbulence Model	Richardson Extrapolation ($C_{f,h=0}$)	GCI (%)
SA	$5.682 \cdot 10^{-3}$	0.963%
k-ω SST	$4.730 \cdot 10^{-3}$	1.052%

In Figure 3, it can be seen that the skin friction coefficient obtained with the SA model is decreases with the grid refinement while the opposite is true for k-ω SST turbulence model. The experimental data for C_f at this particular location is within the range of 5.2–5.6 (x10^{-3}) in different experiments. Therefore, it is appropriate to conclude that the SA model predicts the C_f better than the k-ω SST turbulence model. In conclusion, grid convergence is achieved within the asymptotic range of convergence for both engineering turbulence models, thus the medium grid level is sufficient for further simulations of the two-dimensional impinging SWTBLI problem using a Reynolds-averaged turbulence modeling approach.
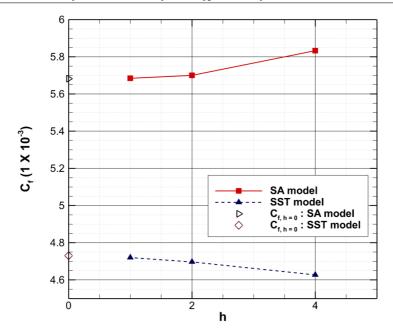
Figure 3. The obtained numerical values of the skin friction coefficient C_f and the Richardson extrapolation ($C_{f,h=0}$) for $\beta = 10°$

4. RESULTS AND DISCUSSION

In this section, the compressible solver of the SU2 open-source code is utilized to analyze a Mach number 5 flow for a 2D impinging SWTBLI where different shock generator angles are investigated in comparison with the experimental data of Schülein et al. [27] and computational data by Leger and Poggie [31, 32]. The medium grid level is assumed to be appropriate for the validation of the results.

4.1. **Weak interaction case ($\beta = 6°$).** At $\beta = 6°$, a weak interaction event has been modeled and good agreement between CFD and experimental data is achieved for both the SA and k-ω SST turbulence models, including parameters such as skin friction, wall pressure and boundary layer profiles. In Figure 4, the skin friction coefficient C_f is plotted along the flat plate at $\beta=6°$. Previous experimental data and CFD results are also plotted as reference data for comparison. From the skin friction plot, as expected for a weak interaction case, no flow separation is predicted by all approaches, except for the k-ω SST model, where a very small separation region is observed. Better agreement is observed before the shock impingement region as compared to after it at the location $x = 0.350\ m$. A drop in skin friction values is observed, as expected from [29] however, the location of such drop is different for each turbulence model. This drop in skin friction is predicted to be the earliest at around x≈0.330 m with the k-ω SST model, followed by the SA model at x≈0.336

m. A quantitatively smaller drop in skin friction is modeled with the SA model, as the one-equation model is more resistant to flow separation and change in wall shear stress.
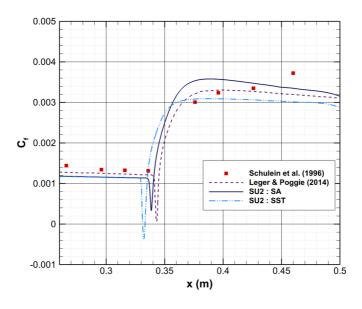
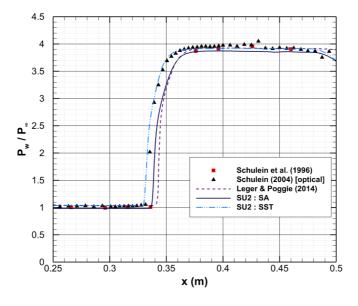

Figure 4. Skin friction distribution for $\beta = 6°$

Figure 5. Wall pressure distribution for $\beta = 6°$

Figure 5 presents the wall pressure p_w distribution on the flat plate for β=6° where both turbulence models provide good agreement. A pressure jump is predicted in both cases; pressure change with the k-ω SST model (x $\approx$ 0.331 m) is very close to that of the experimental data of Schülein et al. [27]. Pressure rise is over-predicted by the SA model at the location of x $\approx$ 0.337 m whereas the Negative SA model (SA-neg) [29] predicts it at the location of x $\approx$ 0.342 m. Across the pressure jump near the interaction point, pressure ratios in all cases are estimated to be within the range, $p_3/p_1 \approx$ 3.865-3.913. This is close to the value reported by Brown [18] which is $p_3/p_1 \approx$ 3.762. A pressure plateau region is observed after the interaction point, which shows close agreement with the experimental data of Schülein et al. [27].

In Figure 4, it can be observed that the C_f profile after the shock impingement is not in very close agreement with the experimental data. This could be due to the turbulence models being incapable of modeling the boundary layer recovery accurately despite this, the order of magnitude is captured reasonably well. On the other hand in Figure 5, close agreement can be seen between the pressure profiles before and after the shock impingement. This trend has been observed in all three angles of attacks and is visible in the plots below. At all three shock generator angles, dimensionless velocity profiles are investigated at different sections as reported by Schülein et al. [27]. All of the sections are located downstream of the interaction point where the compression waves are formed. For all sections, the typical trend of the viscous sublayer and the log-layer in a turbulent boundary layer is modeled by both turbulence models. However, within the log-layer, a close fit between experimental data and the law of the wall curve is not observed. Besides, the transition from log-layer to defect-layer at all sections predicted by both models with the use of the SU2 code is not closely matched with the measurements of Schülein et al. [27]. At a location furthest away from the interaction point, the best match between the k-ω SST dimensionless velocity profile and experimental data is shown in Figure 6. This is possibly due to the flow behavior at the location, which is least affected by compression waves and the shock formation. Discrepancies between experimental and CFD results can be due to the poor performance of the Reynolds-averaged turbulence modeling approach in accounting for non-equilibrium viscous behaviour and complex shock system.

At a fixed streamwise range, density contours computed with the SU2 code are further compared along with the Schlieren visualization by Schülein et al. [27] in Figure 7. The shock impingement point is predicted slightly earlier at x $\approx$ 0.330 m with the k-ω SST model while a later point is predicted at the location of x $\approx$ 0.336 m with the SA model. In comparison with reference data, earlier interaction between incidence shock and turbulent boundary layer is predicted by both turbulence models available in the SU2 compressible fluid flow solver. The SU2 code can predict general flow topology such as incidence and reflected shocks at $\beta = 6°$.
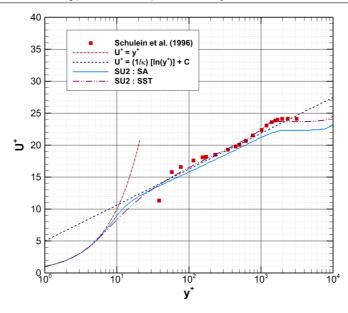
Figure 6. Dimensionless velocity profile for $\beta = 6°$ at x $= 0.460$ m

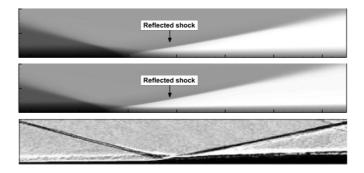Figure 7. Density contours in comparison with the Schlieren visualization for $\beta = 6°$ (from top to bottom: SU2 SA model, SU2 k-ω SST model and the experiment of Schülein et al. [27])

4.2. **Incipient interaction case ($\beta = 10°$).** Figure 8 presents the skin friction coefficients C_f as computed at $\beta = 10°$ in comparison with the experimental data of Schülein et al. [27], and CFD data taken from the NASA Wind-US code and from Leger and Poggie [31, 32]. The results are similar for different approaches, except for the interaction region in the range of 0.321 $m < x < 0.350$ m. Downstream of the location x ≈ 0.350 m, the skin friction plateau level is underpredicted by CFD simulations of the Wind-US, US3D and SU2 codes. The SA model of the SU2 code

shows better agreement with the experimental data within this region. However, it is possible that the uncertainties associated with the experimental data of Schülein et al. [27] cause such discrepancies. In terms of the slope associated with the rise in the skin friction after the shock interaction, the trend predicted by the SU2 code is closely fitted with that of experimental data (see Figure 8). Overall, the skin friction distribution over the flat plate is well modeled by the SU2 compressible fluid flow solver, except for the shock interaction and separation zones.
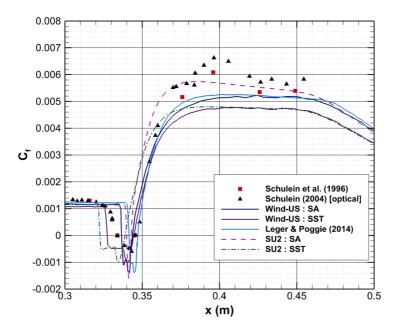

Figure 8. Skin friction distribution for $\beta = 10°$

Within the shock interaction region, flow separation is predicted with the SA and the k-ω SST turbulence models using the SU2 code. Based on the results from the Wind-US and the SU2 codes, an earlier flow separation is observed in the case of the k-ω SST model as compared to that of the SA model. As experimental measurements lead to a flow separation at x ≈ 0.334 m, the Mach number 5 flow over the flat plate separates at x ≈ 0.322 m in the case of the k-ω SST model while delayed flow separation is predicted at x ≈ 0.340 m with the SA model. In comparison with the experimental data of Schülein et al. [27] at x ≈ 0.345 m, reattachment points occur earlier in the case of the k-ω SST model at x ≈ 0.339 m and at around x ≈ 0.343 m with the SA model. Separation bubble size is predicted by the SA model to be about one-third of the experimental value, which is significantly smaller than the value predicted with the k-ω SST model (50% greater in size in comparison with the experimental data). The results are consistent with those reported in the literature [27], where the flow separation is underestimated by the SA model and overestimated with the k-ω SST

model. The discrepancies between these results are possibly due to the limitations of the Reynolds-averaged modeling in flows with complex shock formation and thermo-chemical effects.

Wall pressure distribution p_w at $\beta = 10°$ is plotted in Figure 9. Close agreement is obtained with both turbulence models investigated here for the wall pressure distribution. Pressure rise is predicted to be the earliest with the k-ω SST model at x ≈ 0.321 m, followed by the SA model and the SA-neg model, which computes a later pressure jump at x ≈ 0.340 m than in the experiments at x ≈ 0.332 m. The Pressure plateau level after the interaction point is computed to be around $p_3/p_1 \approx 7.65$-7.71, which is similar to that reported by Brown [18], $p_3/p_1 \approx 7.63$. The pressure distributions are captured very well in comparison with experimental data, and it can be concluded that the Reynolds-averaged modeling approach in the SU2 code is capable of calculating accurate wall pressure distribution p_w for a moderate interaction event involving an impinging SWTBLI on a flat plate at Mach number of 5.
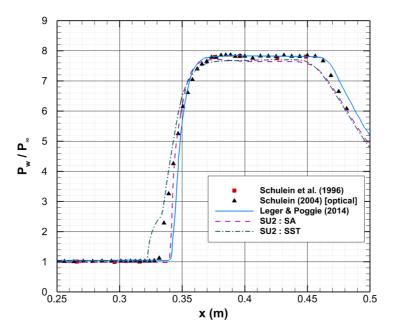

Figure 9. Wall pressure distribution for $\beta = 10°$

The dimensionless velocity profile for $\beta = 10°$ is plotted in Figure 10. Within the viscous sublayer, the curves modeled by both turbulence models investigated here are in agreement with the profile of $U^+ = y^+$. The CFD results as computed by the SU2 code are also closely matched with the law of the wall at all sections. However, experimental values are observed to be slightly deviated from the law of the wall. The main discrepancy between experimental and the CFD dimensionless velocity profiles is found within the defect-layer. In this region, the k-ω SST model is deduced to be

superior to the SA model in predicting the flow behavior of SWTBLI case at Mach number of 5. Dimensionless velocity profiles of the k-ω SST model are quite similar to those obtained in the experiments at all sections, with only a slight difference in the transition from the log-layer to the defect-layer.
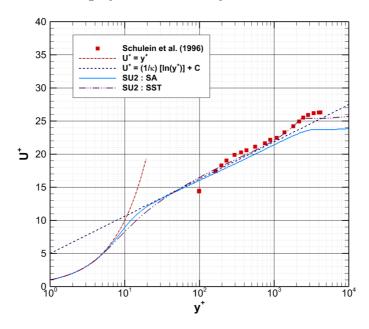

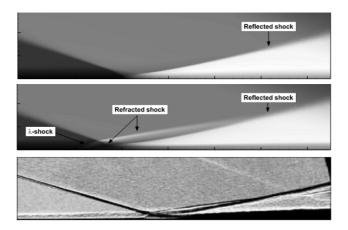Figure 10. Dimensionless velocity profile for $\beta = 10°$ at x = 0.460 m

Figure 11. Density contours in comparison with the Schlieren visualization for $\beta = 10°$ (from top to bottom: SU2 SA model, SU2 k-ω SST model and the experiment of Schülein et al. [27])

In Figure 11, the density fields computed by the SU2 solver are generated compared to the Schlieren images from the experiment [27]. The formation of two refracted shocks from the incidence shock and the λ-shock upstream of the separation region can be observed from the density contour of the k-ω SST model. Two refracted shocks are created when expansion waves are formed as oblique shock penetrates the separation bubble. Reflected shock is then formed from the merging of both refracted shocks and compression waves downstream of the interaction point. The type of shocks observed in the Schlieren images are consistent with that predicted with the k-ω SST model. Only reflected shock is observed in the density field of the SA model due to its small separation bubble size. In addition, the separation region is predicted to begin earlier with the k-ω SST model, as it is known to overestimate separation size.
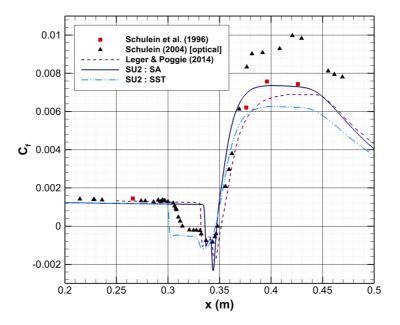

Figure 12. Skin friction distribution for $\beta = 14°$

4.3. **Strong interaction case ($\beta = 14°$).** A strong interaction case at $\beta = 14°$ is investigated in this subsection. The discrepancy between experimental and computational results is found to be the most significant at this angle. Figure 12 presents the skin friction coefficients C_f over the flat plate, plotted with reference to experimental and CFD data taken from the literature [27, 31, 32]. In this case, the extent of the shock interaction is much greater than at $\beta = 10°$, which spans a range of $0.300 \ m < x < 0.350 \ m$. As the interaction strength is the strongest at $\beta = 14°$, the discrepancies between experimental and computational results are more significant. Downstream of the interaction region, skin friction values are underestimated with all CFD approaches employed here. The SA model of the SU2 code predicts the skin

friction plateau level closest to the experimental data of Schülein et al. [27]. The skin friction is observed to increase at the same rate for both experimental and CFD curves. Separation points are estimated at x ≈ 0.336 m and x ≈ 0.301 m with the SA and the k-ω SST models, respectively. In comparison with the experimental data of Schülein et al. [27] at x ≈ 0.314 m, early flow separation is predicted with the k-ω SST model, while separation predicted with the SA model is delayed. Close agreement is obtained by both turbulence models for reattachment points at x ≈ 0.347 m. Separation and reattachment points predicted by the SA and the SA-neg model are observed to be similar. The separation bubble observed in the SA model is one-third that of the experiment, while separation bubble size predicted with the k-ω SST model is about 40% larger than the experimental data in [27]. This could be due to the nature of the SA model in underestimating wall shear stress, while excessive turbulence kinetic energy might be modeled with the k-ω SST model in this case.
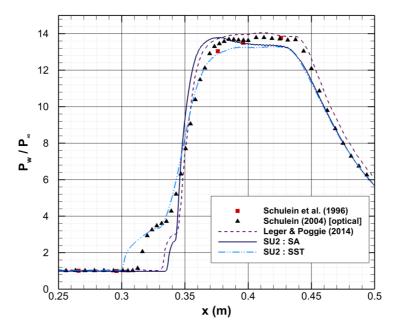

Figure 13. Wall pressure distribution for $\beta = 14°$

In Figure 13, the wall pressure distribution p_w across the flat plate at $\beta = 14°$ is plotted along with the experimental data [27]. In this case, greater discrepancy in data is observed downstream of the shock interaction region due to the strong interaction strength. Wall pressure values are slightly underestimated post-interaction by both turbulence models. Initial pressure jumps are estimated at x ≈ 0.335 m and x ≈ 0.300 m with the SA and the k-ω SST models, while x ≈ 0.313 m is measured in the experiment. A second inflection point at $p_w/p_\infty \approx 3.71$-$4.02$ is observed with the k-ω SST model at x ≈ 0.335 m, which coincides with the experimental data. In
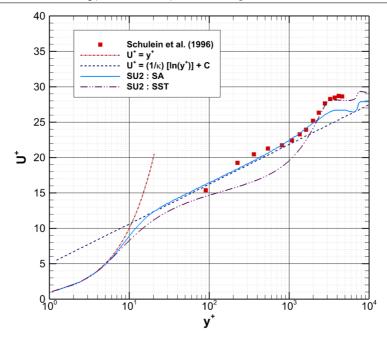
Figure 14. Dimensionless velocity profile for $\beta = 14°$ at x = 0.460 m

contrast, a second inflection point is predicted at a lower pressure, $p_w/p_\infty \approx 2.71$, x ≈ 0.343 m. Therefore, better agreement is achieved by the k-ω SST model as compared to the SA model. The pressure plateau level downstream of interaction region at $\beta = 14°$ is computed about $p_3/p_1 \approx 13.25$-13.44, while it is reported by Brown [18] as $p_3/p_1 \approx 13.62$. As compared to the results at $\beta = 10°$, the difference in pressure plateau levels is slightly greater at $\beta = 14°$. This is due to poor performance of the typical Reynolds-averaged modeling in simulations involving significant flow separation and pressure change across the shock interaction zone.

In Figure 14, the velocity profile of the k-ω SST model is observed to deviate from the law of the wall; however, the transition predicted from the log-layer to the defect-layer is consistent with experimental measurements [27]. The velocity profile of the SA model follows the law of the wall, although it fails to predict correctly the defect-layer at this location. In the sections further downstream of the shock impingement point, modeled boundary layer profiles are fairly close to the experimental data with differences for the defect-layer. It can be concluded that the transition from the log-layer to the defect-layer is poorly estimated by both turbulence models in a strong interaction case. This is due to the assumptions made in the turbulence models that simplify flow problems based on subsonic benchmark test cases which do not include the shock interaction. In future studies, the role of coefficients and functions in URANS modeling can also be investigated.
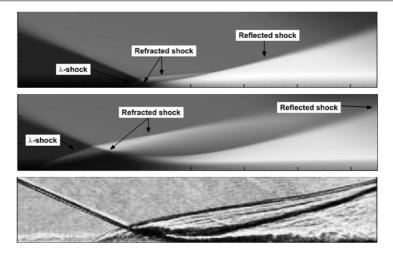
Figure 15. Density contours in comparison with the Schlieren visualization for $\beta = 14°$ (from top to bottom: SU2 SA model, SU2 k-ω SST model and the experiment of Schülein et al. [27])

The simulated density fields are plotted with the Schlieren images in Figure 15. Flow separation is predicted to be earlier in the k-ω SST model, while it is delayed in the SA model. Separation size in the k-ω SST is around 50% larger than in the experiment [27], while the SA model gives a separation region which is half of that. Two refracted shocks observed with the k-ω SST model are more distinct than with the SA model, where weaker shocks are formed instead. In addition, expansion waves spanning from one of the refracted shock are clearly shown in the density contour of the k-ω SST model. The density field of the k-ω SST model closely resembles the structure of the shock system observed in the experiment, including the angles of the λ-shock foot and refracted shocks formed at the triple point. It can be concluded that the SA model is unable to predict the degree of flow separation and SWTBLI in a strong interaction case, whereas the k-ω SST model tends to overestimate the separation size and produce stronger shocks in the flow field.

5. Conclusions and Future Work

The open source SU2 CFD code has been evaluated in this study at a Mach number of 5 where an impinging SWTBLI on a flat plate is investigated and compared to the experimental data of Schülein et al. [27]. The results presented demonstrate the strengths and weakness of the SU2 code for the investigation of such a high Mach number flow. For the 2D impinging SWTBLI case, the SA and the k-ω SST turbulence models are used to compute the flow field. These turbulence modeling approaches were validated against the experimental data for parameters such as skin friction, wall pressure distribution and boundary layer profiles. The discrepancies between computational and experimental data become more significant with higher

shock generator angles β, which indicates increasing shock interaction strength. It can also be observed that neither turbulence model was capable of capturing the boundary layer recovery after the shock impingement, which resulted in discrepancy in the results for C_f. However, pressure profiles were captured very well for all three angles. Both turbulence models are concluded to be less reliable within the shock interaction and separation regions. This is due to the inherent working principle of Reynolds-averaged modeling, which does not resolve small and large scale eddies in the flow field. At all β angles, earlier flow separation is predicted with the k-ω SST model, while the flow field is less sensitive to separation for SU2 simulations with the SA model. The SA model is deduced to be better in the prediction of reattachment points, while the complex shock system at higher β angles is better computed by the k-ω SST model. A larger separation size and stronger shock formation are predicted with the k-ω SST model as compared to the SA model. With both turbulence models Wall pressure distributions are captured well within the experimental values. Velocity profile results are plotted to be less accurate in comparison with experimental data at higher β values. Although the SA model predicts better velocity curves at some sections, both turbulence models are unable to solve the SWTBLI case with high reliability and accuracy for a strong interaction case. Based on the evaluation of the SU2 open-source code for the Schülein et al. [27] case, the compressible solver is found to be suitable for a preliminary or rough assessment of high Mach flows with SWTBLI phenomenon in the industry. However, for research purposes, more sophisticated three-dimensional unsteady turbulence modeling approaches such as LES and DES should be included in the SU2 solver. Moreover, other cases with high Mach number flows and SWTBLI such as compression ramps or double fins can be taken as further validation steps for the current SU2 solver.

References

1. Cecere, D., Ingenito, A., Romagnosi, L., Bruno, C. and Giacomazzi, E.: Shock/boundary layer/heat release interaction in the HyShot II scramjet combustor. In *Proceedings of 46th AIAA Joint Propulsion Conference & Exhibit*, Nashville, TN, USA, 2010. DOI: 10.2514/6.2010-7066

2. Segal, C.: In The Scramjet Engine: Processes and Characteristics. *Cambridge University Press*, 2009, ISBN 9780511627019. DOI: 10.1017/CBO9780511627019

3. Schetz, J. A., and Billig, F. S.: Studies of scramjet flowfields. In *Proceedings of 23rd AIAA Joint Propulsion Conference*, San Diego, California, USA, 1987. DOI: 10.2514/6.1987-2161

4. SMART, M. K., HASS, N. E. AND PAULL, A.: Flight data analysis of the HyShot 2 scramjet flight experiment. *AIAA Journal*, **44**(10), (2006), 2366–2375. DOI: 10.2514/1.20661

5. MASS, N. E., SMART, M. K. AND PAULL, A.: Flight data analysis of HyShot 2. In *A Collection of Technical Papers–13th AIAA/CIRA International Space Planes and Hypersonic Systems and Technologies Conference*, Vol. 2, 2005. DOI: 10.2514/6.2005-3354

6. LAURENCE, S., SCHRAMM, J. M., KARL, S. AND HANNEMANN, K.: An experimental investigation of steady and unsteady combustion phenomena in the HyShot II combustor. In *Proceedings of 17th AIAA International Space Planes and Hypersonic Systems and Technologies Conference*, 2011, p. 14. DOI: 10.2514/6.2011-2310

7. KARL, S., HANNEMANN, K., MACK, A. AND STEELANT, J.: CFD analysis of the HyShot II scramjet experiments in the HEG shock tunnel. In *Proceedings of 15th AIAA International Space Planes and Hypersonic Systems and Technologies Conference*, American Institute of Aeronautics and Astronautics, USA, 2008, p. 16. DOI: 10.2514/6.2008-2548

8. BERGLUND, M. AND FUREBY, C.: LES of supersonic combustion in a scramjet engine model. *Proceedings of the Combustion Institute*, **31**(2), (2007), 2497–2504. DOI: 10.1016/j.proci.2006.07.074

9. FUREBY, C., CHAPUIS, M., FEDINA, E. AND KARL, S.: CFD analysis of the HyShot II scramjet combustor. *Proceedings of the Combustion Institute*, **33**(2), (2011), 2399–2405. DOI: 10.1016/j.proci.2010.07.055

10. CHAPUIS, M., FEDINA, E., FUREBY, C., HANNEMANN, K., KARL, S. AND SCHRAMM, J. M.: A computational study of the HyShot II combustor performance. *Proceedings of the Combustion Institute*, **34**(2), (2013), 2101–2109. DOI: 10.1016/j.proci.2012.07.014

11. YOU, Y., LUEDEKE, H. AND HANNEMANN, K.: Injection and mixing in a scramjet combustor: DES and RANS studies. *Proceedings of the Combustion Institute*, **34**(2), (2013), 2083–2092. DOI: 10.1016/j.proci.2012.10.001

12. KARL, S., LAURENCE, S., SCHRAMM, J. M. AND HANNEMANN, K.: CFD analysis of unsteady combustion phenomena in the HyShot-II scramjet configuration. In *Proceedings of 18th AIAA/3AF International Space Planes and Hypersonic Systems and Technologies Conference*, American Institute of Aeronautics and Astronautics, USA, 2012, p. 13. DOI: 10.2514/6.2012-5912

13. WEN, C. Y., CHEN, Y. S. AND CHEN, J. Y.: Numerical simulation of complex internal viscous flow in the HyShot-II scramjet model. In *Proceedings of 17th AIAA International Space Planes and Hypersonic Systems and Technologies Conference*, American Institute of Aeronautics and Astronautics, USA, 2011, p. 9. DOI: 10.2514/6.2011-2382

14. PECNIK, R., TERRAPON, V. E., HAM, F., IACCARINO, G. AND PITSCH, H.: Reynolds–Averaged Navier–Stokes simulations of the HyShot II scramjet. *AIAA Journal*, **50**(8), (2012), 1717–1732. DOI: 10.2514/1.J051473

15. BEN-YAKAR, A; MUNGAL, G. AND HANSON, R.: Time evolution and mixing characteristics of hydrogen and ethylene transverse jets in supersonic crossflows. *Physics of Fluids*, **18**(2), (2006), 315–323. DOI: 10.1063/1.2139684

16. RANA, Z. A., THORNBER, B. AND DRIKAKIS, D.: Transverse jet injection into a supersonic turbulent cross-flow. *Physics of Fluids*, **23**(4), (2011), 046103. DOI: 10.1063/1.3570692

17. RANA, Z. A., THORNBER, B. AND DRIKAKIS, D.: Dynamics of sonic hydrogen injection and mixing inside scramjet combustor. *Engineering Applications of Computational Fluid Mechanics*, **7**(1), (2013), 13–39. DOI: 10.1080/19942060.2013.11015451

18. BROWN, J.: Shock wave impingement on boundary layers at hypersonic speeds: computational analysis and uncertainty. In *Proceedings of 42nd AIAA Thermophysics Conference*, American Institute of Aeronautics and Astronautics, USA, 2011, p. 63. DOI: 10.2514/6.2011-3143

19. GAITONDE, D. V.: Progress in shock wave/boundary layer interactions. *Progress in Aerospace Sciences*, **72**, (2015), 80–99. DOI: 10.1016/j.paerosci.2014.09.002

20. TITCHENER, N. AND BABINSKY, H.: Shock wave/boundary-layer interaction control using a combination of vortex generators and bleed. *AIAA Journal*, **51**(5), (2013), 1221–1233. DOI: 10.2514/1.J052079

21. DOLLING, D. S.: Fifty years of shock-wave/boundary-layer interaction research: What next? *AIAA Journal*, **39**(8), (2001), 1517–1531. DOI: 10.2514/2.1476

22. FANG, J., YAO, Y., ZHELTOVODOV, A., LI, Z. AND LU, L.: Direct numerical simulation of supersonic turbulent flows around a tandem expansion-compression corner. *Physics of Fluids*, **27**(12), (2015), 125104. DOI: 10.1063/1.4936576

23. KNIGHT, D., YAN, H., PANARAS, A. AND ZHELTOVODOV, A.: Advances in CFD prediction of shock wave turbulent boundary layer interactions. *Progress in Aerospace Sciences*, **39**(2–3), (2003), 121–184. DOI: 10.1016/S0376-0421(02)00069-6

24. DUSSAUGE, J. - P.; DUPONT, P. AND DEBIÈVE, J. - F.: Unsteadiness in shock wave boundary layer interactions with separation. *Aerospace Science and Technology*, **10**(2), (2006), 85–91. DOI: 10.1016/j.ast.2005.09.006

25. PIROZZOLI, S. AND BERNARDINI, M.: Direct numerical simulation database for impinging shock wave/turbulent boundary-layer interaction. *AIAA Journal*, **49**(6), (2011), 1307–1312. DOI: 10.2514/1.J050901

26. DIOP, M., PIPONNIAU, S., AND PIERRE, D.: On the length and time scales of a laminar shock wave boundary layer interaction. In *Proceedings of 54th AIAA Aerospace Sciences Meeting*, American Institute of Aeronautics and Astronautics, USA, 2016, p. 18. DOI: 10.2514/6.2016-0073

27. SCHÜLEIN, E., KROGMANN, P. AND STANEWSKY, E.: Documentation of two-dimensional impinging shock/turbulent boundary layer interaction flow. *DLR report 223-96 A49, 69S*, 1996. DOI: https://elib.dlr.de/37537/

28. SETTLES, G. S. AND DODSON, L. J.: Supersonic and hypersonic shock/boundary-layer interaction database. *AIAA Journal*, **32**(7), (1994), 1377–1383. DOI: 10.2514/3.12205

29. SETTLES, G. S. AND DODSON, L. J.: Hypersonic shock/boundary-layer interaction database. In *Proceedings of 22nd Fluid Dynamics, Plasma Dynamics and Lasers Conference*, Honolulu, HI, USA, 1991. DOI: 10.2514/6.1991-1763

30. FEDOROVA, N. N. AND FEDORCHENKO, I. A.: Computations of interaction of an incident oblique shock wave with a turbulent boundary layer on a flat plate. *Journal of Applied Mechanics and Technical Physics*, **45**(3), (2004), 358–366. DOI: 10.1023/B:JAMT.0000025017.49191.14

31. LEGER, T. J. AND POGGIE, J.: Computational analysis of shock wave turbulent boundary layer interaction. In *Proceedings of 52nd Aerospace Sciences Meeting*, American Institute of Aeronautics and Astronautics, USA, 2014. DOI: 10.2514/6.2014-0951

32. LEGER, T., BISEK, N. AND POGGIE, J.: Computations of turbulent flow over a sharp fin at Mach 5. *Journal of Thermophysics and Heat Transfer*, **30**(2), (2016), 394–402. DOI: 10.2514/1.T4698

33. FANG, J., YAO, Y., ZHELTOVODOV, A. A. AND LU, L.: Numerical simulations of two-dimensional and three-dimensional shock wave/turbulent boundary layer interactions. In *ICMAR 2014*, Novosibirsk, Russia, 2014. DOI: http://eprints.uwe.ac.uk/24250

34. PALACIOS, F., ECONOMON, T. D., ARANAKE, A., COPELAND, S. R., LONKAR, A., LUKACZYK, T., MANOSALVAS, D., NAIK, K., PADRON, S., TRACEY, B., VARIYAR, A. AND ALONSO, J.: Stanford University Unstructured (SU2): analysis and design technology for turbulent flows. In *Proceedings of 52nd Aerospace Sciences Meeting, AIAA SciTech Forum*, American Institute of Aeronautics and Astronautics, USA, 2014-0243. DOI: 10.2514/6.2014-0243

35. PALACIOS, F., ALONSO, J., COLONNO, M., ARANAKE, A., CAMPOS, A., COPELAND, S., ECONOMON, T., LONKAR, A., LUKACZYK, T. AND TAYLOR, T.: Stanford University Unstructured (SU2): An open source integrated computational environment for multiphysics simulation and design. In *Proceedings of 51st AIAA Aerospace Sciences Meeting including the New Horizons Forum and Aerospace Exposition, Aerospace Sciences Meetings*, American Institute of Aeronautics and Astronautics, USA, 2013. DOI: 10.2514/6.2013-287

36. ECONOMON, T., MUDIGERE, D., BANSAL, G., HEINECKE, A., PALACIOS, F., PARK, J., SMELYANSKIY, M., ALONSO, J. AND DUBEY, P.: Performance optimizations for scalable implicit RANS calculations with SU2. *Computers & Fluids*, **129**, (2016), 146–158. DOI: 10.1016/j.compfluid.2016.02.003

37. SPALART, P. AND ALLMARAS, S.: A one-equation turbulence model for aerodynamic flows. In *Proceedings of 30th Aerospace Sciences Meeting and Exhibit, Aerospace Sciences Meetings*, Reno, NV, USA, 1992. DOI: 10.2514/6.1992-439

38. MENTER, F. R.: Two-equation eddy-viscosity turbulence models for engineering applications. *AIAA Journal*, **32**(8), (1994), 1598–1605. DOI: 10.2514/3.12149

39. CHORIN, A. J.: A numerical method for solving incompressible viscous flow problems. *Journal of Computational Physics*, **135**(2), (1997), 118–125. DOI: 10.1006/jcph.1997.5716

40. WILCOX, D. C.: *Turbulence Modeling for CFD*. DCW industries La Canada, CA, 1998, ISBN-10: 1928729088.

41. VENKATAKRISHNAN, V.: Convergence to steady state solutions of the euler equations on unstructured grids with limiters. *Journal of Computational Physics*, **118**(1), (1995), 120–130. DOI: 10.1006/jcph.1995.1084

42. ROACHE, P. J.: *Verification and Validation in Computational Science and Engineering*. Hermosa Publishers, Albuquerque, New Mexico, 1998, ISBN-10: 0913478083.

43. AIAA: Guide for the Verification and Validation of Computational Fluid Dynamics Simulations. *AIAA G-077-1998*, 1998, eISBN: 978-1-56347-285-5. DOI: 10.2514/4.472855

44. Schülein, E.: Skin friction and heat flux measurements in shock/boundary layer interaction flows. *AIAA Journal*, **44**(8), (2006), 1732–1741. DOI: 10.2514/1.15110